Materials & Design 226 (2023) 111560

Contents lists available at ScienceDirect

Materials & Design

journal homepage: www.elsevier.com/locate/matdes

An inverse design paradigm of multi-functional elastic metasurface via data-driven machine learning

Weijian Zhou [a,b], Shuoyuan Wang [c], Qian Wu [d], Xianchen Xu [d], Xinjing Huang [c], Guoliang Huang [d,*], Yang Liu [c,*], Zheng Fan [a,*]

[a] School of Mechanical and Aerospace Engineering, Nanyang Technological University, 50 Nanyang Avenue, Singapore 639798, Singapore
[b] School of Science, Harbin Institute of Technology, Shenzhen 518055, China
[c] State Key Laboratory of Precision Measuring Technology and Instruments, Tianjin University, Tianjin 300072, China
[d] Department of Mechanical and Aerospace Engineering, University of Missouri, Columbia, MO 65211, USA

HIGHLIGHTS

- Propose a data-driven inverse design paradigm of multifunctional elastic metasurface.
- Demonstrating a dual-functional metasurface with defection and focusing at different frequencies.

GRAPHICAL ABSTRACT

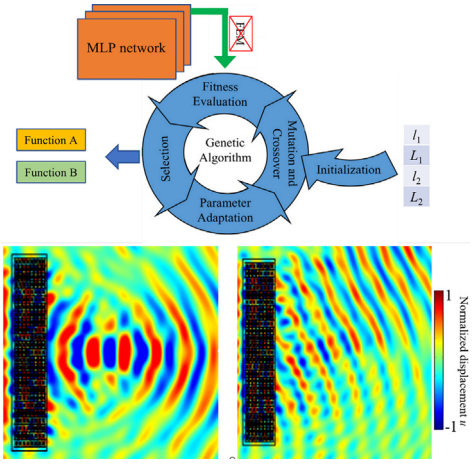

ARTICLE INFO

Article history:
Received 18 September 2022
Revised 9 December 2022
Accepted 29 December 2022
Available online 4 January 2023

Keywords:
Acoustic metasurface
Multi-functional
Inverse design
Machine learning
Data-driven

ABSTRACT

Elastic metasurfaces have become one of the most promising platforms for manipulating mechanical wavefronts with the striking feature of ultra-thin geometry. The conventional design of mechanical metasurfaces significantly relies on numerical, trial-and-error methods to identify structural parameters of the unit cells, which requires huge computational resources and could be extremely challenging if the metasurface is multi-functional. Machine learning technique provides another powerful tool for the design of multi-functional elastic metasurfaces because of its excellent capability in building nonlinear mapping relation between high-dimensional input data and output data. In this paper, a machine learning network is introduced to extract the complex relation between high-dimensional geometrical parameters of the metasurface unit and its high-dimensional dynamic properties. Based on a big dataset, the well-trained network can play the role of a surrogate model in the inverse design of a multi-functional elastic metasurface to significantly shorten the time for the design. Such method can be conveniently extended to design other multi-functional metasurfaces for the manipulation of optical, acoustical or mechanical waves.

* Corresponding authors.
E-mail addresses: huangg@missouri.edu (G. Huang), ultrasonicslab@tju.edu.cn (Y. Liu), ZFAN@ntu.edu.sg (Z. Fan).

https://doi.org/10.1016/j.matdes.2022.111560
0264-1275/

1. Introduction

Precise wavefront manipulation of acoustic and elastic waves is of great significance in both academic and industrial communities. However, due to the mass law, traditional low-frequency wavefront manipulation with natural materials suffers from bulky geometry. This problem can be well addressed by the application of mechanical metasurface, a low-dimensional mechanical metamaterial [1–6]. While a carefully designed metasurface element can provide a local phase shift to the incoming wave, a series of such metasurface elements can realize a certain phase profile, achieving arbitrary manipulation of the wavefront through generalized Snell's law.

The concept of metasurface was first proposed in the field of optics. Yu et al. [7] designed a dielectric optical antenna which can fulfill, based on its geometry, a full 2π phase shift span for both reflected and refracted light waves. An array of such antennas with subwavelength separation and carefully designed phase distribution form a gradient metasurface with excellent wavefront regulation performance for both reflected and refracted waves. This concept was then extended to the field of acoustics and has subsequently led to the development of labyrinthine [8,9], Helmholtz resonant [10] and adjacent-wave-coupling [11] acoustic metasurfaces. Acoustic metasurfaces have shown excellent subwavelength wave manipulation functions, including near or far field focusing, transmission deflection, total reflection, planar diffuser, etc. [12–14]. In the comparison with the optical and the acoustic predecessors, wavefront manipulation of elastic wave requires much more complicated designs, mainly due to the nature of modal coupling of elastic waves [15–17]. The local phase shift of the elastic wave depends mainly on the propagation distance and the wave velocity in the metasurface element. The labyrinth metasurface is designed based on the modulation of propagation distance [18]. Thus far, most of the existing elastic metasurfaces were designed based on either mass or stiffness modulation to cover a full 2π phase shift span [18–20]. In those designs, the impedances of the metasurfaces are generally not considered, resulting in low transmission of the waves. The impedance of a metasurface element is related to the multiplication of its effective mass and stiffness. Thus, simultaneously controlling the effective mass and stiffness can be a solution to achieve 2π local phase control while maintaining high transmission ratio. Based on this principle, Lee et al. proposed a mass-stiffness substructuring method to design elastic metasurfaces, demonstrating beam steering and focusing functions for longitudinal waves with nearly perfect transmission condition [21]. The metasurface element includes two independent mass and stiffness substructures, responsible for generating independently tailorable effective mass density M_{eff} and stiffness K_{eff}, respectively. Consequently, the element can realize simultaneously a 2π local phase shift span (phase velocity $v \sim \sqrt{K_{eff}/M_{eff}}$) and high transmission (impedance matching $Z \sim K_{eff}M_{eff}$) at certain frequencies. However, the search of optimal design parameters for such metasurfaces highly relies on a cumbersome, repeated parameter-sweep process and inefficient post processing of the simulation data. Furthermore, it can be extremely difficult to deal with higher-dimensional problems, especially for the designing of multi-functional metasurfaces [22–24]. One way to tackle this issue is to utilize the topological optimization algorithm and search for multiple objects [25–27]. However, in these optimization scenarios, a huge number of finite element method (FEM) simulations are required in each generation, making the inverse design inevitably cumbersome and time-consuming. As a result, the conventional optimization method is far from optimal for the design of multi-functional metasurfaces.

Recent development of artificial intelligence reveals that machine learning technique can serve as a powerful tool in building nonlinear mapping relation between high-dimensional input and output data, making it an excellent candidate in designing multi-functional metasurfaces. In 2006, Hinton and Salakhutdinov found that multilayer neural network has excellent feature extraction ability, facilitating the rapid development of machine learning [28]. The essence of machine learning is an interconnected multilayer nonlinear neural network. To mine the inherent correlation involved in the training data, a mapping relationship between the input and output layers can be established by using a back-propagation algorithm. Due to its powerful feature extraction performance, data fitting, and high-dimensional data processing capability, machine learning has been successfully applied in many fields such as language and speech processing [29,30], visual recognition [31,32], pharmaceutical field [33] and financial field [34]. For example, the deep learning was employed to design the metasurface for the absorption of microwaves [35]. However, its application in mechanical systems is still in its infancy, and there have been few relevant research achievements reported yet. Li et al. [36] combined autoencoder and multilayer perceptron to achieve a reverse mapping from a band structure to a mechanical structure. Zhu et al. [37] used pre-trained Inception V3 network for migration training to rapidly predict acoustic metasurface phase transition parameters. Zhang et al. [38] applied generative adversarial network (GAN) to the rapid generation of mechanical metamaterials with good noise reduction. Recently, Yaw et al. [39] employed machine learning for the design of a novel elastic metasurface to convert longitudinal waves to SV waves with high efficiency. All these works have confirmed that the machine learning approach possesses excellent high-dimensional modeling capabilities.

In this paper, we employ the machine learning approach to establish the mapping from the high-dimensional geometrical parameters of an elastic metasurface to its high-dimensional dynamic parameters: transmission coefficients and local phase shifts for various frequencies. Based on the resulting forward mapping network, we propose a fast data-driven inverse design method for the realizations of a single-functional metasurface, which executes beam deflection, and a dual-functional metasurface, which demonstrates focusing and beam deflection functions at distinct frequencies. High accuracy of the network is observed, and the designing time required for both types of metasurfaces can range from several seconds to several minutes, depending on the dimension of the designing target. The use of the proposed machine learning technique greatly reduces computational resources when compared with other optimization approaches. Therefore, the proposed machine-learning-based design principle can serve as a versatile platform for the design of next-generation multi-functional metasurface in engineering applications.

2. Inverse design of multi-functional elastic metasurface

According to Lee et al. [21], high transmission is achievable with the independent modulation of the effective stiffness and mass of a metasurface element. Here we use a similar element design to construct the dual-functional metasurface, with its unit cell shown in Fig. 1. For easier fabrication, chamfering is introduced to the structure. In the unit cell, the groove lengths l and L control the effective stiffness and effective mass, respectively. The width of the grooves is 0.5 mm.

As multiple degrees of freedom are required by the dual functions, we combine two metasurfaces, with each composed of four-unit cells (Fig. 2). The two metasurfaces are denoted by "1"

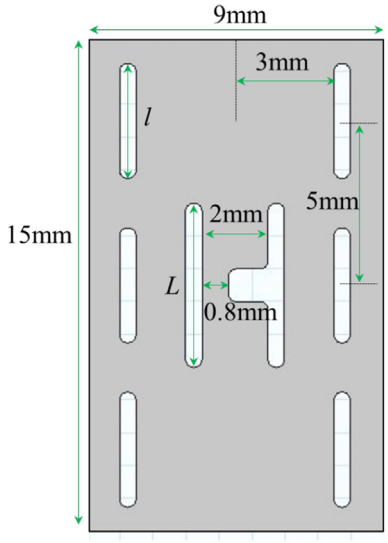

Fig. 1. The structure of the unit cell.

and "2". The lengths of their respective grooves are represented by l_i and L_i $(i = 1, 2)$. The geometrical parameters are input into the commercial FEM software COMSOL Multiphysics to simulate the transmission coefficients T_i $(i = 1, 2)$ in the frequency domain. 3×10^5 FEM simulations are conducted to collect the transmission coefficients to form an output dataset, and the corresponding geometrical parameters are collected as an input dataset, after which the input and output dataset are inserted into a Multi-Layer Perceptron (MLP) network to mine the complex relation between the geometrical parameters and the transmission characteristics.

We excited longitudinal waves on the left of the metasurface at frequencies $f_1 = 80$kHz and $f_2 = 100$kHz. Due to the existence of the metasurface unit, there exist two kinds of waves in the left background: incident and reflected waves. According to Ref [2], the wave transmission T can be obtained as

$$T = \frac{2u_R}{1 + iu_L} \tag{1}$$

in which $i = \sqrt{-1}$, u_R being the output longitudinal displacement on the right of the metasurface, and u_L is the longitudinal displacement measured at a point $\lambda/4$ far away from the excitation, with λ being the operating wavelength.

We randomly generated 3×10^5 groups of geometrical parameters and imposed these data to COMSOL Multiphysics to conduct FEM simulations in the frequency domain. Then we collected the data set including the transmission T_1 for the frequency f_1 and T_2 for f_2. Subsequently, we used 70 % of them for learning, 15 % for validation and the rest for testing. Since the network can only deal with real-valued data, we separated the complex transmissions T_1 and T_2 into four groups, i.e., $\mathrm{Re}(T_1)$, $\mathrm{Im}(T_1)$, $\mathrm{Re}(T_2)$ and $\mathrm{Im}(T_2)$. This new data set was then employed in the training of the deep learning network formed by a four-component input layer, a $30 \times 30 \times 30 \times 30 \times 30$ hidden layer, and a four-component output layer. The *fitnet* program in MATLAB was used to build and train the network with a Levenberg-Marquardt back-propagation optimizer. The training ratio was set as 0.01. This network was then trained to learn the mapping functions $T_1(l_1, L_1, l_2, L_2)$ and $T_2(l_1, L_1, l_2, L_2)$.

When randomly generating the geometrical parameters, we set a constraint to the generator. For instance, the real part of the transmission $T_1(l_1, L_1, l_1, L_1)$ is shown in Fig. 3. We can see that in some areas the mapping verifies smoothly with respect to l_1 and L_1. However, in certain areas this mapping changes sharply, requiring more data points in these areas. Therefore, we divided the total sweeping domain of (l_1, L_1) into six subdomains as shown in Fig. 3. Similar data distribution is obtained for geometrical parameters l_2 and L_2.

The training process is shown in Fig. 4(a), with the green circle standing for the stopping point: the training stops when the validation minimum mean square error (MSE) (the green solid line) cannot become smaller in the following 6 steps. We can see that the network is well trained. The MSE of the validation reaches 5.55×10^{-4}. We choose 1000 data from the testing dataset to check the accuracy of the network. The histogram of the relative error defined as $|(T_{prediction} - T_{FEM})/T_{FEM}|$ is shown in Fig. 4(b), from which we can see that about 95.7 % of the prediction errors are within 1 %, which means our network can accurately predict the transmission coefficient and local phase shift once the geometrical parameters l and L are given. We also plot the transmission coefficient and local

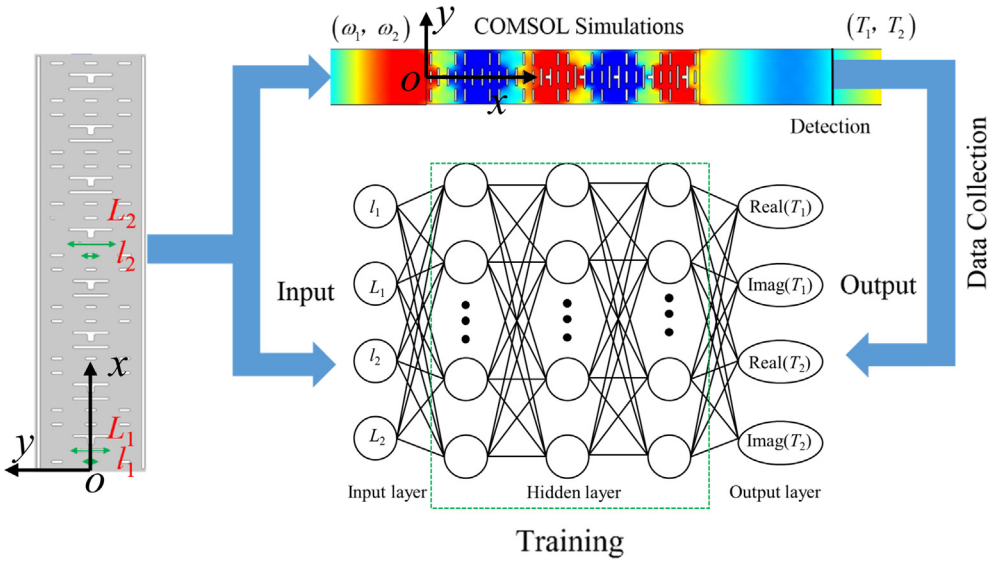

Fig. 2. Geometry of the metasurface and the sketch of the machine learning network.

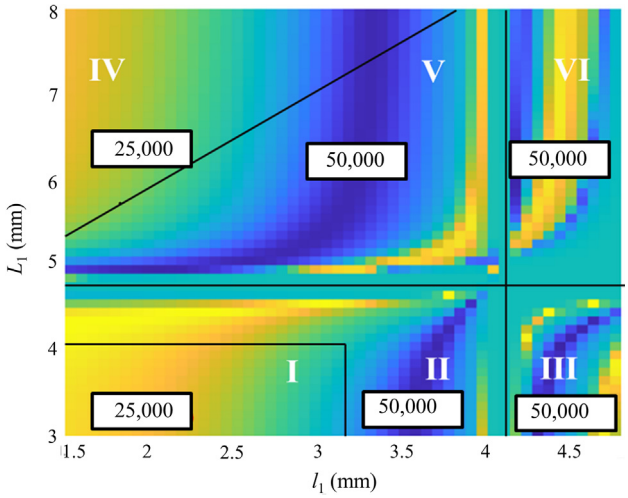

Fig. 3. Real part of transmission parameter T_1 as a function of l_1 and L_1. The distribution of data is also presented, with the color standing for the real part of T_1. The values in the blocks represent the numbers of the generated geometric data.

phase shift of these 1000 testing data in Fig. 4(c) and 4(d), respectively. The cycle marks represent the prediction result from the network, while the star marks are for the true results from FEM simulations. We can observe that the predicted results match very well with the simulation results. Again, this proves that the network can accurately predict the transmission parameters of the metasurface and is a proper candidate for design of metasurface.

2.1. Inverse design of mechanical metasurface

In a traditional inverse design of multi-functional metasurface based on topological optimization, hundreds of generations are needed. In each generation, from tens to thousands of FEM simulations are required to be conducted, making the traditional optimization of multi-functional metasurface extremely cumbersome. To overcome this problem, we propose to use the well-trained network as a surrogate model to replace the time-consuming FEM simulations in each optimization generation as shown in Fig. 5. By doing so, we can inversely obtain the desired geometrical parameters within a short time after providing a target phase profile.

It should be noted that the data collection for deep learning costs a long time, but this can be easily accelerated by using parallel simulations. In fact, we conducted tens of COMSOL simulations simultaneously. Subsequently, the training and application for inverse design is fast. Let us consider a scenario when we first inversely design a metasurface for a certain function and then the design changes. The convolutional optimization method needs to completely repeat the heavy simulation. However, for the inverse design based on deep learning, the data collection does not need to be repeated, leading to extremely fast design of the new metasurface. This highlights the advantage of the inverse design method proposed in our paper.

2.2. Inverse design of a single-functional mechanical metasurface

Our design method can be easily applied to design a single-functional elastic metasurface. Let us consider the design of a pla-

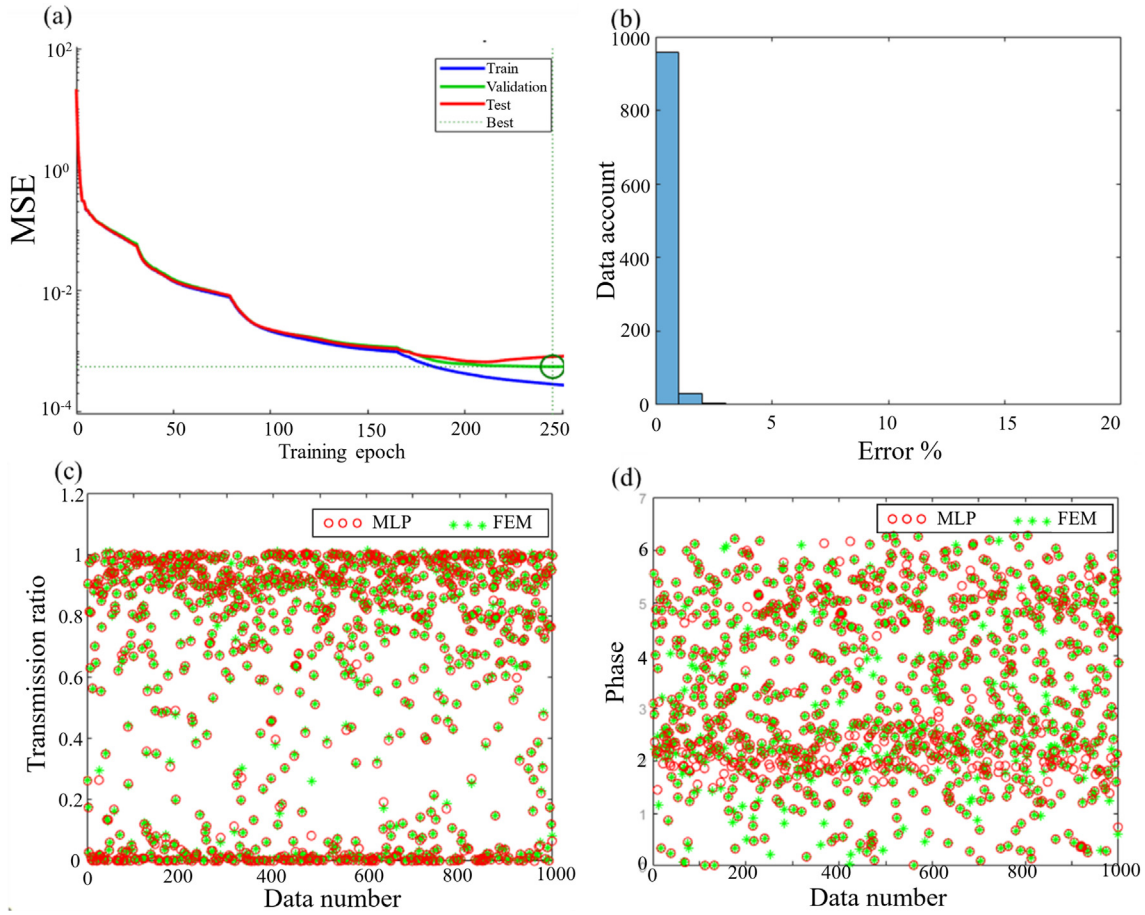

Fig. 4. (a) Training process; (b) Histogram of prediction error of the network; (c) and (d): comparison between network prediction and the FEM simulation.

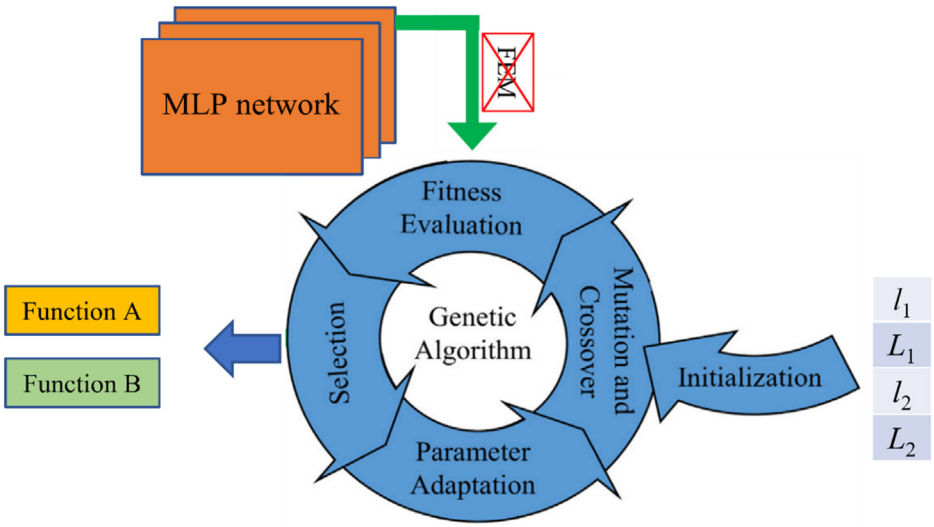

Fig. 5. Schematic of the machine learning network as a surrogate model to inversely design the dual-functional metasurface element. The fitness evaluation that contains a large number of FEM simulations is improved by replacing these FEM simulations by fast prediction of MLP network, making the inverse design fast and accurate.

nar metasurface lens for far field focusing. The phase profile of the lens is

$$\varphi(y) = k_0\left(\sqrt{f_L^2 + y^2} - f_L\right) \tag{2}$$

where $k_0 = 2\pi/\lambda_L$, λ_L is the longitudinal wavelength at 100 kHz, and f_L is the focal length of the lens. We set $f_L = 0.15m$, and the target phase profile is shown as the black solid curve in Fig. 6(a). Based on the well-trained network, we can obtain the desired structural parameters of the metasurface elements, whose transmission coefficient is larger than 0.9, and the true phase profile calculated from COMSOL Multiphysics is plotted as red star marks in Fig. 6(a). We can see that the red marks exactly overlap with the target phase profile, meaning that the network accurately predicts the transmission performance of the metasurface. We then input these geometrical parameters into COMSOL Multiphysics and conduct the corresponding simulation. As shown in Fig. 6(b), a line excitation locates at the left boundary of the thin plate (of 0.5 mm thickness), and perfect matched layers (PMLs) are designated for the other three boundaries. The color stands for the strain energy distribution of the wave field, from which we can see the transmitted waves are focused at a point about 0.15 m away from the metasurface, agreeing well with our design target.

2.3. Inverse design of dual functional mechanical metasurface

For the design of a dual-functional elastic metasurface, we set the transmission limit as 0.85, meaning that the transmission coefficients at frequencies 80 kHz and 100 kHz are larger than 0.85. As an example, we obtain a 6-bits metasurface elements as a fundamental base to design the dual-functional metasurface (see Table A1 in Appendix). The 6-bits fundamental base consists of 8×8 elements. It takes a few minutes to establish the whole database. The phases and transmission coefficients of this 6-bit base are shown in Fig. 7(a) for 80 kHz and Fig. 7(b) for 100 kHz. The transmission coefficients highlighted in green are very close to 1. Moreover, the cycles are the phases from network prediction, while the stars are from FEM simulations. Good agreement can be seen between the network prediction and FEM simulations.

First, let us consider the dual-functional deflection function. Our design target is for the metasurface to exhibit deflection angles of 30^0 at 80 kHz and of -30^0 at 100 kHz. As is shown in Fig. 8(a) and 8

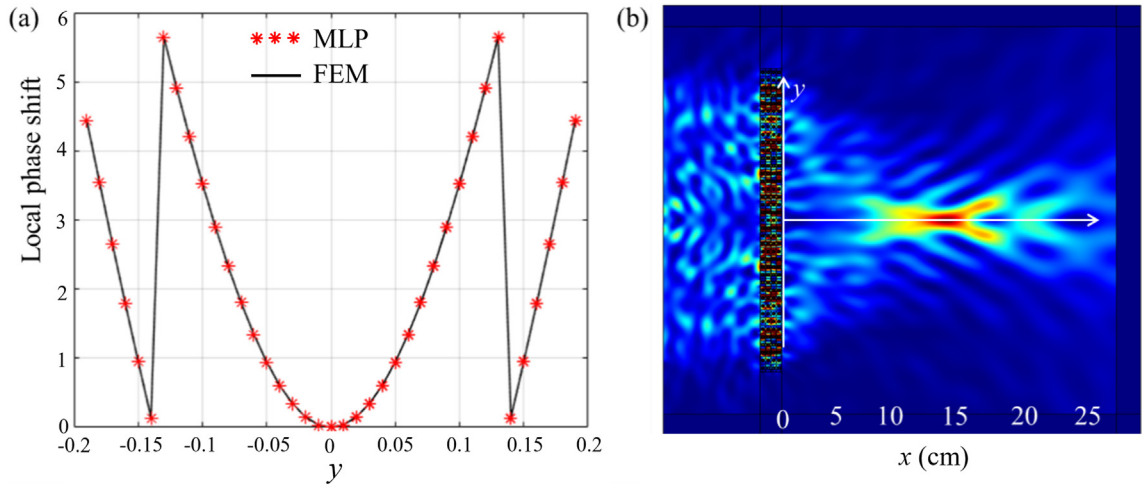

Fig. 6. (a) Phase profile of the planar lens and (b) strain energy distribution of the planar lens.

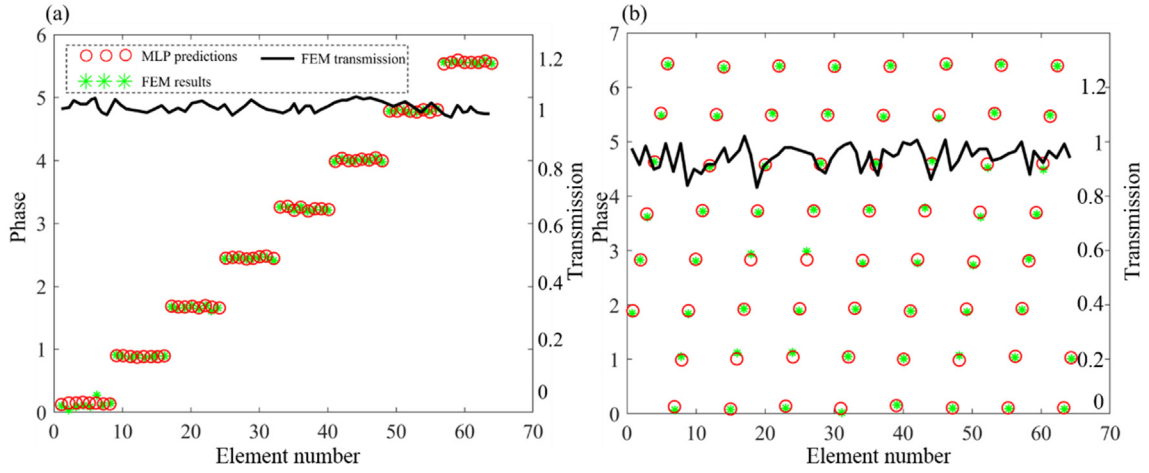

Fig. 7. Dynamic parameters of the 6-bits base for (a) 80 kHz and (b) 100 kHz.

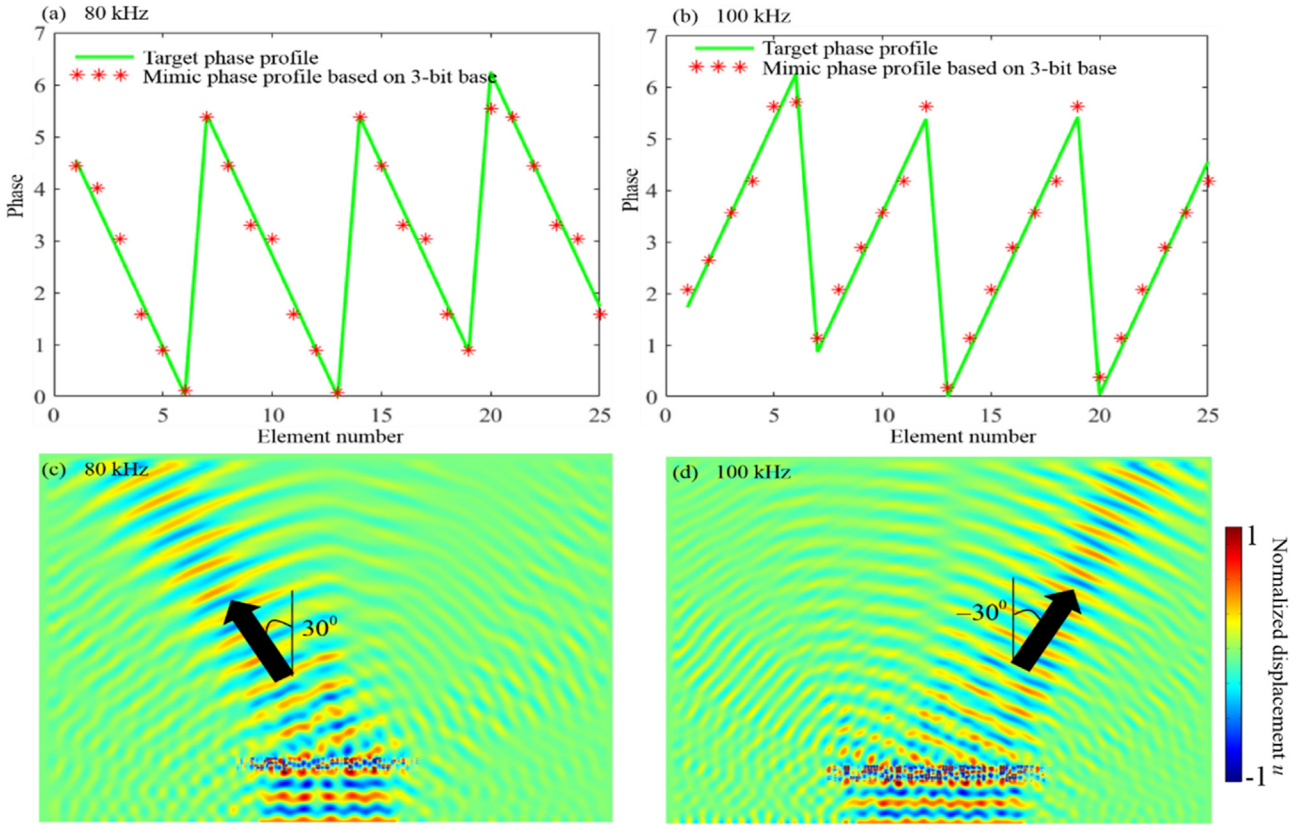

Fig. 8. Dual-functional metasurface realizing deflection of 30° at 80 kHz and deflection of −30° at 100 kHz. (a) The phase profile at 80 kHz. (b) The phase profile at 100 kHz. (c) The numerically obtained longitudinal displacement field at 80 kHz; (d) The numerically obtained longitudinal displacement field at 100 kHz.

(b), we use the 6-bit base to mimic the target phase profile of the deflection, i.e.

$$\varphi_{80}(y) = \frac{2\pi}{\lambda_{80}} sin(-\pi/3)y,$$

$$\varphi_{100}(y) = \frac{2\pi}{\lambda_{100}} sin(\pi/3)y. \quad (3)$$

Here λ_{80} and λ_{100} are the longitudinal wavelengths at 80 kHz and 100 kHz, respectively. Then the corresponding geometrical parameters are inserted into numerical simulations to attain the frequency responses. The displacement fields at 80 kHz and 100 kHz are shown in Fig. 8(c) and 8(d), from which we clearly see the dual-functional deflection, with the distinguishable deflection angles of 30^0 at 80 kHz and of -30^0 at 100 kHz.

Next, we consider a dual-functional metasurface behaving as a planar lens at 80 kHz and wave deflector at 100 kHz. The target phase profiles are

$$\varphi_{80}(y) = \frac{2\pi}{\lambda_{80}} \left(\sqrt{f_L^2 + y^2} - f_L \right),$$

$$\varphi_{100}(y) = \frac{2\pi}{\lambda_{100}} sin(\pi/3)y. \quad (4)$$

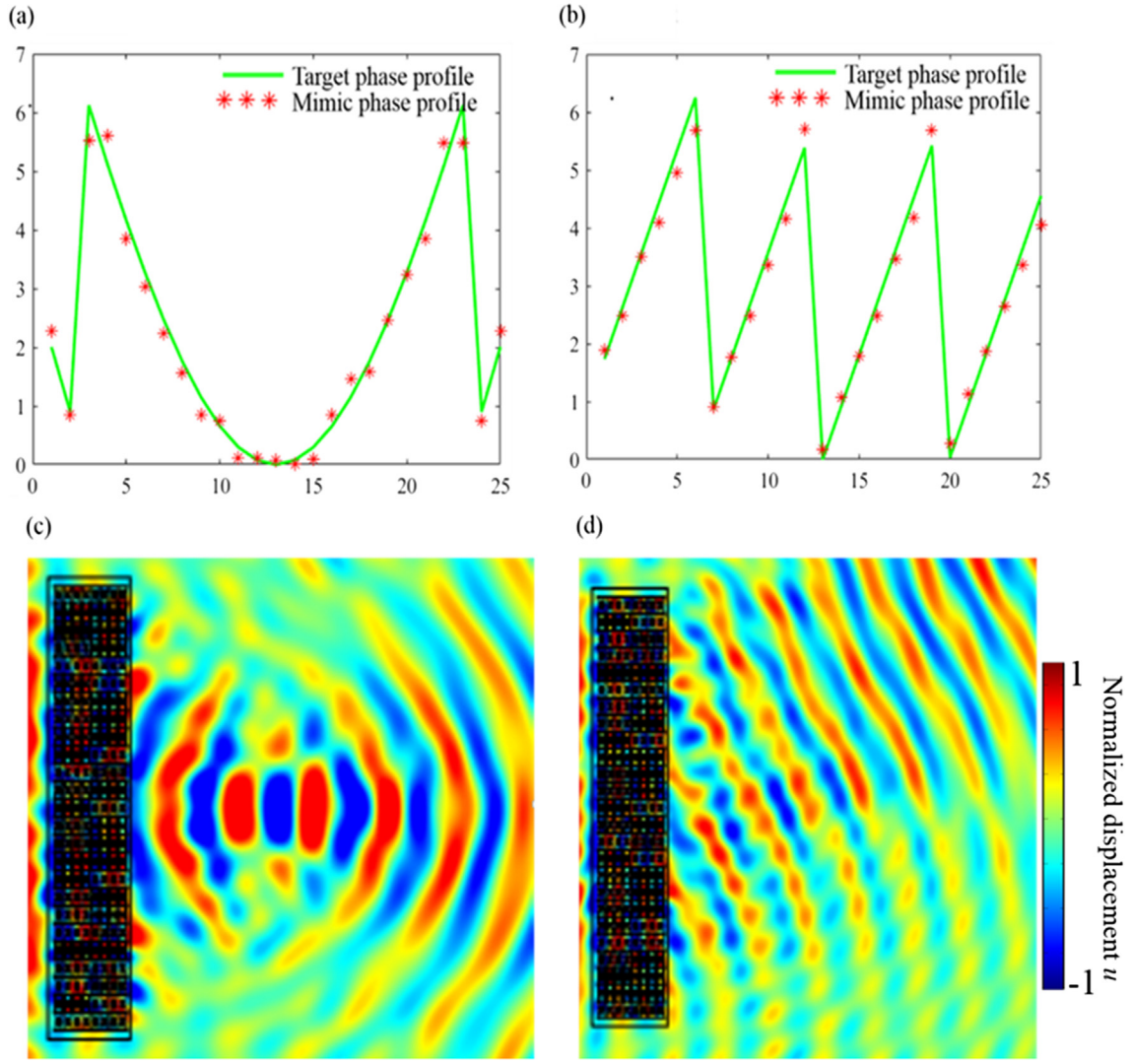

Fig. 9. Dual-functional metasurface composing of planar lens with focusing length 0.12 m at 80 kHz, and deflection 30^0 at 100 kHz. (a) The phase profile at 80 kHz; (b) The phase profile at 100 kHz; (c) the displacement field at 80 kHz; (d) the displacement field at 100 kHz.

Here, $f_L = 0.12m$. We use the 6-bits base to mimic these phase profiles, and the corresponding results are displayed in Fig. 9(a) and 9(b). Then we conduct harmonic simulations to verify our design. The obtained displacement field at 80 kHz, as shown in Fig. 9(c) indicates that the transmitted waves are focused at a point about 0.12 m away from the metasurface, which agrees well with our design target. The displacement field at 100 kHz shown in Fig. 9(d) illustrates the deflection with an angle being about 30^0, again agreeing well with the other design target.

2.4. Experimental validation

In order to verify the beam control capability of our dual-function metasurface, we first fabricate the metasurface structure (380 × 72 × 1 mm) from 6061 thin aluminium plate (800 × 1000 × 1 mm) by precision cutting, with the prototype shown in Fig. 10(a). The reason for using 6061 thin aluminium plate to process metasurface is that the tensile strength σ_b is greater than or equal to 180 MPa, and its yield strength $\sigma_{0.2}$ is greater than or equal to 110 MPa, which has good processing performance and toughness. The minimum size of the metasurface structure was 0.5 mm, and the error of length and width was controlled within 50 μm. The structural parameters of aluminium plate are obtained from our numerical simulations. As shown in Fig. 10(b) and 10(c), the testing system mainly includes a scanning Laser Doppler vibrometer (LDV) system, an aluminium plate with a dual-functional metasurface, a function generator SDG2042X and a power amplifier ATA-3080. To produce a longitudinal plane wave in the aluminium plate, a magnetostrictive transducer was designed and placed on the aluminium plate with an iron-cobalt belt. A magnetic field perpendicular to the plate is applied on the iron-cobalt belt. Thus, the fundamental symmetric Lamb waves (S_0 wave) to mimic the longitudinal wave were excited in aluminium plate by the magnetostrictive effect. To improve the signal-to-noise ratio, the signals are averaged 20 times, and a digital band-pass filter is also implemented.

The wavefields at both frequencies after postprocessing are shown in Fig. 11(a) and 11(b). It can be experimentally observed from Fig. 11(a) that the waves are focused at a point about 0.12 m away from the metasurface. This observation confirms our numerical prediction shown in Fig. 9(c). The wave deflection presented in Fig. 11(b) illustrates a deflection angle of about 30^0, which also agrees well with our numerical prediction given in

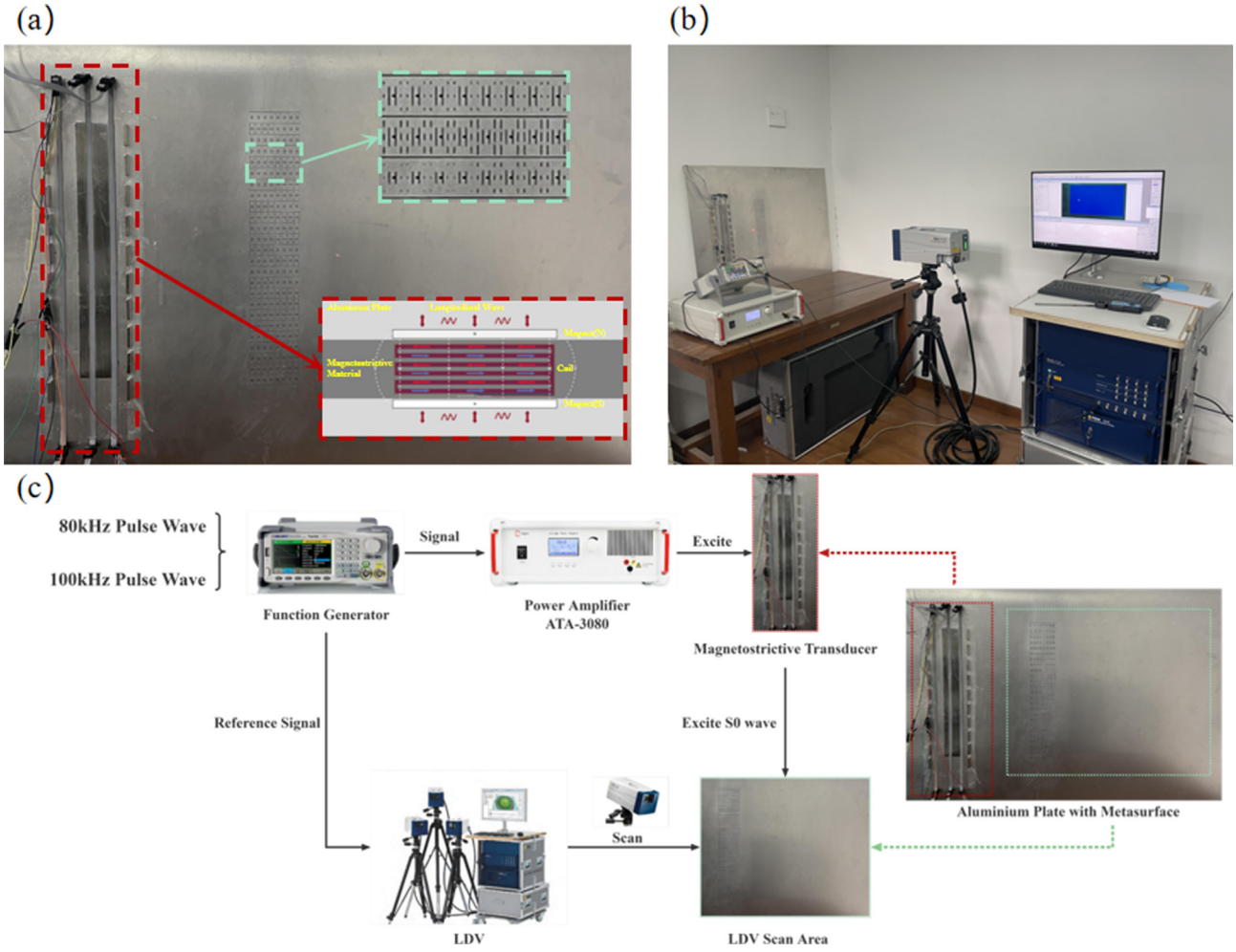

Fig. 10. Experimental set. (a) the prototype of the dual-functional metasurface; (b) experimental platform; (c) the signal generator, transformer, amplifier and detector.

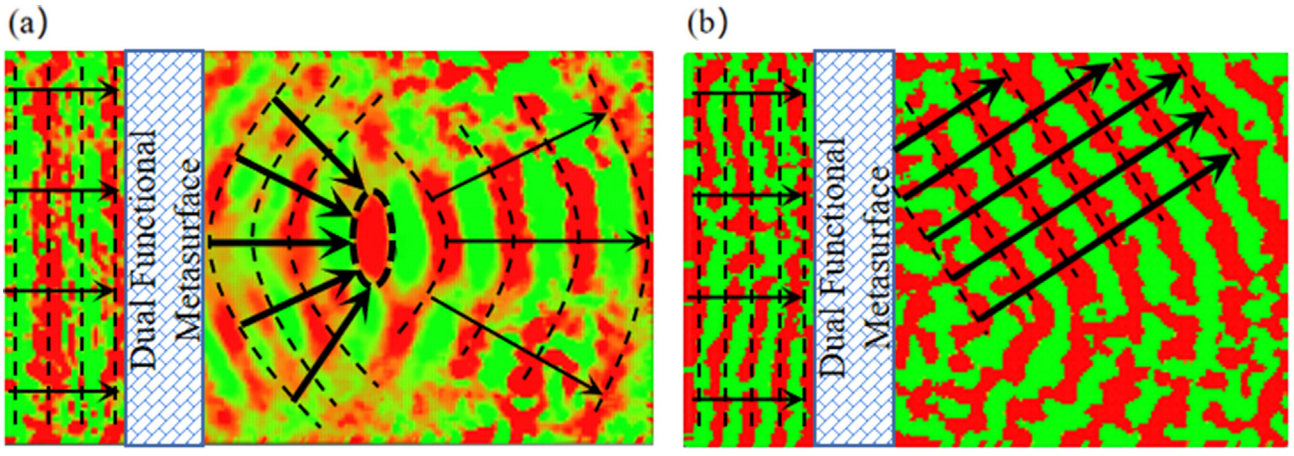

Fig. 11. (a) The experimental displacement field at 80 kHz; (b) the experimental displacement field at 100 kHz.

Fig. 9(d). Overall, our experimental demonstration confirms that the dual-functional metasurface exhibits two different functions, namely focusing at 80 kHz and beam deflection at 100 kHz. More importantly, the dual-functional metasurface can be fast and accurately designed based on the proposed machine learning method.

3. Conclusion

In this paper, we propose to employ the machine learning technique to develop a fast inverse design method for multi-functional elastic metasurface. We start from designing a single functional

metasurface, by using a well-trained network that possesses forward mapping from geometrical parameters of metasurface unit to its dynamic performances as a surrogate model and insert it into exhaust algorithm. By this means, design of an elastic metasurface with 39 units can be completed within two seconds. The prediction from machine learning network agrees very well with FEM simulations, and based on that we design a planar lens. FEM simulations show that the focusing length is exactly our design target.

Then we propose to use machine learning to fast design a dual-functional metasurface. Via big data training, the network can mine the relation between four geometrical parameters and four dynamic parameters, which include transmission ratios and local phase shifts at frequency 80 kHz and 100 kHz. Similar to the surrogate exhaust algorithm, various dual-functional metasurfaces can be fast obtained. As an example, we build a 6-bits design base composing of 64 fundamental units, and it takes about three minutes to complete the simulation. Based on such 3-bits base, the phase profiles of various dual-functional metasurface can be fitted, and then various dual-functional metasurfaces can be realized. As two typical examples, we designed a dual-functional metasurface composing of wave deflection with different angles at two working frequencies, and a metasurface that works as a planar lens at 80 kHz and as wave deflection at 100 kHz. FEM simulations are conducted to verify our design, and good agreement can be observed. We further conducted experimental study to verify the dual-functional composing of planar lens and deflection, and good agreement is also observed.

In conclusion, our method based on machine supports both fast and accurate design of multi-functional metasurface, and it can be easily extended to design higher order multi-functional acoustic/optical/elastic metasurfaces, and thus can also find significant importance in engineering design of elastic metasurfaces.

Data availability

Data will be made available on request.

Declaration of Competing Interest

The authors declare that they have no known competing financial interests or personal relationships that could have appeared to influence the work reported in this paper.

Acknowledgements

The authors would like to acknowledge funding support from the Ministry of Education Singapore under Grant No. MOE2019-T2-2-068, A*STAR Singapore Science and Engineering Research Council under AME Individual Research Grant (IRG) 2018 Grant Call (Project No. A1983c0030), and the funding support from National Natural Science Foundation of China (No. 12202117).

Appendix

See Tables A1.

References

[1] B. Assouar, B. Liang, Y. Wu, Y. Li, J.C. Cheng, Y. Jing, Acoustic metasurfaces, Nat. Rev. Mater. 3 (12) (2018) 460–472.
[2] Z. Yaw, W.J. Zhou, Z. Chen, C.W. Lim, Stiffness tuning of a functional-switchable active coding elastic metasurface, Int. J. Mech. Sci. 207 (2021) 106654.
[3] Z. Yaw, W.J. Zhou, C.W. Lim, Anomalous Wave Control by an Adaptive Elastic Metasurface Shunted with Negative Capacitance Circuit, J. Sound Vib. 116782 (2022).
[4] H.H. Huang, C.T. Sun, G.L. Huang, On the negative effective mass density in acoustic metamaterials, Int. J. Eng. Sci. 47 (4) (2009) 610–617.
[5] T.A.M. Hewage, K.L. Alderson, A. Alderson, F. Scarpa, Double Negative Mechanical Metamaterials Displaying Simultaneous Negative Stiffness and Negative Poisson's Ratio Properties, Adv. Mater. 28 (46) (2016) 10323–10332.
[6] Y.Y. Chen, X.P. Li, G.K. Hu, M.R. Haberman, G.L. Huang, An active mechanical Willis meta-layer with asymmetric polarizabilities, Nature Communication. 11 (2020) 3681.
[7] N.F. Yu, P. Genevet, M.A. Kats, F. Aieta, J.P. Tetienne, F. Capasso, Z. Gaburro, Light propagation with phase discontinuities: generalized laws of reflection and refraction, Science 334 (2011) 333–337.
[8] Y. Zhu, X. Fan, B. Liang, J. Cheng, Y. Jing, Ultrathin acoustic metasurface-based Schroeder diffuser, Phys. Rev. X 7 (2) (2017) 021034.
[9] Y. Li, X. Jiang, R.Q. Li, B. Liang, X.Y. Zou, L.L. Yin, J.C. Cheng, Experimental realization of full control of reflected waves with subwavelength acoustic metasurfaces, Phys. Rev. Appl 2 (6) (2014) 064002.
[10] Y. Zhu, B. Assouar, Multi-functional acoustic metasurface based on an array of Helmholtz resonators, Phys. Rev. B 99 (17) (2019) 174109.
[11] J. Chen, J. Xiao, D. Lisevych, A. Shakouri, Z. Fan, Deep-subwavelength control of acoustic waves in an ultra-compact metasurface lens, Nat. Commun. 9 (1) (2018) 1–9.
[12] Y. Xie, W. Wang, H. Chen, A. Konneker, B.I. Popa, S.A. Cummer, Wavefront modulation and subwavelength diffractive acoustics with an acoustic metasurface, Nat. Commun. 5 (1) (2014) 1–5.
[13] J. Mei, Y. Wu, Controllable transmission and total reflection through an impedance-matched acoustic metasurface, New J. Phys. 16 (12) (2014) 123007.
[14] G. Ma, M. Yang, S. Xiao, Z. Yang, P. Sheng, Acoustic metasurface with hybrid resonances, Nat. Mater. 13 (9) (2014) 873–878.
[15] H. Zhu, F. Semperlotti, Anomalous refraction of acoustic guided waves in solids with geometrically tapered metasurfaces, Phys. Rev. Lett. 117 (3) (2016) 034302.
[16] X.H. Shen, C.T. Sun, M.V. Barnhart, G.L. Huang, Elastic wave manipulation by using a phase-controlling meta-layer, J. Appl. Phys. 123 (2018) 091708.

Table A1
The 6-bits phase base formed by 64 phase elements.

Phase ω_1 Phase ω_2	0 (0, 0, 0)	$\frac{\pi}{4}$ (0, 0, 1)	$\frac{\pi}{2}$ (0, 1, 0)	$\frac{3\pi}{4}$ (0, 1, 1)	π (1, 0, 0)	$\frac{5\pi}{4}$ (1, 0, 1)	$\frac{3\pi}{2}$ (1, 1, 0)	$\frac{7\pi}{4}$ (1, 1, 1)
0 (0, 0, 0)	(0, 0, 0 0, 0, 0)	(0, 0, 1 0, 0, 0)	•	•	•	•	•	(1, 1, 1 0, 0, 0)
$\frac{\pi}{4}$ (0, 0, 1)	(0, 0, 0 0, 0, 1)	(0, 0, 1 0, 0, 1)	•	•	•	•	•	(1, 1, 1 0, 0, 1)
$\frac{\pi}{2}$ (0, 1, 0)	•	•	•	•	•	•	•	•
$\frac{3\pi}{4}$ (0, 1, 1)	•	•	•	•	•	•	•	•
π (1, 0, 0)	•	•	•	•	•	•	•	•
$\frac{5\pi}{4}$ (1, 0, 1)	•	•	•	•	•	•	•	•
$\frac{3\pi}{2}$ (1, 1, 0)	•	•	•	•	•	•	•	•
$\frac{7\pi}{4}$ (1, 1, 1)	(0, 0, 0 1, 1, 1)	•	•	•	•	•	•	(1, 1, 1 1, 1, 1)

[17] Y.Y. Chen, X.P. Li, H. Nassar, G.L. Huang, A programmable metasurface for real time control of broadband elastic rays, Smart Mater. Struct. 27 (2018) 115011.
[18] Y. Liu, Z. Liang, F. Liu, O. Diba, A. Lamb, J. Li, Source illusion devices for flexural lamb waves using elastic metasurfaces, Phys. Rev. Lett. 119 (3) (2017) 034301.
[19] W. Zhou, Z. Fan, Localization and amplification of Rayleigh waves by topological elastic metasurfaces, Smart Mater. Struct. 30 (8) (2021) 084001.
[20] H. Zhu, S. Patnaik, T.F. Walsh, B.H. Jared, F. Semperlotti, Nonlocal elastic metasurfaces: Enabling broadband wave control via intentional nonlocality, Proc. Natl. Acad. Sci. 117 (42) (2020) 26099–26108.
[21] H. Lee, J.K. Lee, H.M. Seung, Y.Y. Kim, Mass-stiffness substructuring of an elastic metasurface for full transmission beam steering, J. Mech. Phys. Solids 112 (2018) 577–593.
[22] H.X. Xu, C.H. Wang, G.W. Hu, Y.Z. Wang, S.W. Tang, Y.J. Huang, X.H. Ling, W. Huang, C.W. Qiu, Spin-Encoded Wavelength-Direction Multitasking Janus Metasurfaces, Adv. Opt. Mater. 9 (2021) 2100190.
[23] H.X. Xu, G.W. Hu, M.H. Jiang, S.W. Tang, Y.Z. Wang, C.H. Wang, Y.J. Huang, X.H. Ling, H.W. Liu, J.F. Zhou, Wavevector and frequency multiplexing performed by a spin-decoupled multichannel metasurface, Adv. Mater. Technol. 5 (2019) 1900710.
[24] H.X. Xu, G.W. Hu, Y. Li, L. Han, J.L. Zhao, Y.M. Sun, F. Yuan, G.M. Wang, Z.H. Jiang, X.H. Ling, T.J. Cui, C.W. Qiu, Interference-assisted kaleidoscopic meta-plexer for arbitrary spin-wavefront manipulation, Nature Light: Sci. Appl. 8 (2019) 3.
[25] J. Rong, W. Ye, Multi-functional elastic metasurface design with topology optimization, Acta Mater. 185 (2020) 382–399.
[26] J. Rong, W. Ye, S. Zhang, Y. Liu, Frequency-coded passive multi-functional elastic metasurfaces, Adv. Funct. Mater. 30 (50) (2020) 2005285.
[27] K. Miyata, Y. Noguchi, T. Yamada, K. Izui, S. Nishiwaki, Optimum design of a multi-functional acoustic metasurface using topology optimization based on Zwicker's loudness model, Comput. Methods Appl. Mech. Eng. 331 (2018) 116–137.
[28] G.E. Hinton, R.R. Salakhutdinov, Reducing the dimensionality of data with neural networks, Science 313 (5786) (2006) 504–507.
[29] W. Xiong, J. Droppo, X. Huang, F. Seide, M. Seltzer, A. Stolcke, G. Zweig, Achieving human parity in conversational speech recognition, arXiv preprint arXiv, 2016, 1610.05256.
[30] C.C. Chiu, T.N. Sainath, Y. Wu, R. Prabhavalkar, P. Nguyen, Z. Chen, M. Bacchiani, State-of-the-art speech recognition with sequence-to-sequence models, in: 2018 IEEE International Conference on Acoustics, Speech and Signal Processing (ICASSP), 2018, pp. 4774-4778.
[31] Z. Cheng, Q. Yang, B. Sheng, Deep colorization, In Proceedings of the IEEE international conference on computer vision (2015) 415–423.
[32] L.A. Gatys, A.S. Ecker, M. Bethge, Image style transfer using convolutional neural networks, In Proceedings of the IEEE conference on computer vision and pattern recognition (2016) 2414–2423.
[33] E. Gawehn, J.A. Hiss, G. Schneider, Deep learning in drug discovery, Mol. Inf. 35 (1) (2016) 3–14.
[34] J.B. Heaton, N.G. Polson, J.H. Witte, Deep learning for finance: deep portfolios, Appl. Stoch. Model. Bus. Ind. 33 (1) (2017) 3–12.
[35] B.R. Wu, G.M. Wang, K.P. Liu, G.W. Hu, H.X. Xu, Equivalent-circuit-intervened deep learning metasurface 218 (2022) 110725.
[36] X. Li, S. Ning, Z. Liu, Z. Yan, C. Luo, Z. Zhuang, Designing phononic crystal with anticipated band gap through a deep learning based data-driven method, Comput. Methods Appl. Mech. Eng. 361 (2020) 112737.
[37] R. Zhu, T. Qiu, J. Wang, S. Sui, C. Hao, T. Liu, S. Qu, Phase-to-pattern inverse design paradigm for fast realization of functional metasurfaces via transfer learning, Nat. Commun. 12 (1) (2021) 1–10.
[38] H. Zhang, Y. Wang, H. Zhao, K. Lu, D. Yu, J. Wen, Accelerated topological design of metaporous materials of broadband sound absorption performance by generative adversarial networks, Mater. Des. 207 (2021) 109855.
[39] Z. Yaw, C.W. Lim, Z. Zhong, W.J. Zhou, High efficiency generation of S-wave via a transmissive binary coding metasurface based on machine learning approach, Eng. Struct. 272 (2022) 114918.